AGU PUBLICATIONS

JGR

Journal of Geophysical Research: Atmospheres

RESEARCH ARTICLE
10.1002/2015JD023996

Key Points:
- Daytime LSTs were derived from aircraft LSTs and a diurnal temperature cycle model
- Aircraft/satellite LSTs were overall anticorrelated with vegetation indexes
- WRF model performance depended on its setup and varied by location and time

Supporting Information:
- Figures S1–S3

Correspondence to:
M. Huang,
mhuang10@gmu.edu

Citation:
Huang, M., P. Lee, R. McNider, J. Crawford, E. Buzay, J. Barrick, Y. Liu, and P. Krishnan (2016), Temporal and spatial variability of daytime land surface temperature in Houston: Comparing DISCOVER-AQ aircraft observations with the WRF model and satellites, *J. Geophys. Res. Atmos.*, *121*, 185–195, doi:10.1002/2015JD023996.

Received 27 JUL 2015
Accepted 10 DEC 2015
Accepted article online 15 DEC 2015
Published online 14 JAN 2016

Temporal and spatial variability of daytime land surface temperature in Houston: Comparing DISCOVER-AQ aircraft observations with the WRF model and satellites

Min Huang[1,2], Pius Lee[1], Richard McNider[3], James Crawford[4], Eric Buzay[5], John Barrick[4,6], Yuling Liu[7], and Praveena Krishnan[8,9]

[1]NOAA/OAR/ARL Headquarter, College Park, Maryland, USA, [2]Center for Spatial Information Science and Systems, George Mason University, Fairfax, Virginia, USA, [3]Earth System Science Center, University of Alabama, Huntsville, Alabama, USA, [4]NASA Langley Research Center, Hampton, Virginia, USA, [5]National Suborbital Education and Research Center, University of North Dakota, Grand Forks, North Dakota, USA, [6]Science Systems and Applications, Inc., Hampton, Virginia, USA, [7]NOAA/NESDIS and University of Maryland, College Park, Maryland, USA, [8]NOAA/OAR/ARL, Atmospheric Turbulence and Diffusion Division, Oak Ridge, Tennessee, USA, [9]Oak Ridge Associated Universities, Oak Ridge, Tennessee, USA

Abstract Based on a semiempirical diurnal temperature cycle model and aircraft observations taken at different times of the day, daytime land surface temperature (LST) is derived at six locations in the Greater Houston area on the least cloudy day during NASA's DISCOVER-AQ (Deriving Information on Surface Conditions from Column and Vertically Resolved Observations Relevant to Air Quality) field campaign in September 2013. The aircraft-derived daytime LSTs show ranges (max-min) of 11–25°K varying by location, with the daily maxima occurring near 1300–1400 local time. Two Weather Research and Forecasting model simulations that were configured differently are compared with these aircraft-derived LST, indicating location- and time-dependent performance. The NOAA GOES geostationary satellite observed similar LST spatial patterns in Houston to those in finer resolution from two polar-orbiting satellite instruments (Moderate Resolution Imaging Spectroradiometer and Visible Infrared Imaging Radiometer Suite), and it provided useful information of the LST temporal variability missing from the polar-orbiting satellite products. However, spatial- and time-varying discrepancies are found among LSTs from these various platforms, which are worth further evaluation in order to benefit model evaluation and improvement. The aircraft and satellite LSTs are overall anticorrelated with satellite vegetation indexes. This emphasizes the importance of vegetation cover in urban planning due to its cooling effect and further impact on biogenic emissions and regional air quality. The approaches shown in this study are also suitable for applications under cloudless conditions at other locations and times, such as during the remaining DISCOVER-AQ deployments conducted in three other populated regions with diverse land uses.

1. Introduction

Land surface temperature (LST), the temperature of the interface between the Earth's surface and its atmosphere, is an important indicator of the greenhouse effect and the energy flux between the atmosphere and the ground [*Mannstein*, 1987]. LST presents strong spatial heterogeneity and temporal variability, which depend on solar radiation, land surface properties (e.g., land cover types, vegetation and soil conditions, and surface albedo), and the atmospheric conditions such as water vapor and clouds [*Vinnikov et al.*, 2008; *Duan et al.*, 2014; *Jin and Dickinson*, 2010]. Being complemented by the surface air temperature measured at ~2 m above the ground, LST as well as its temporal evolution (e.g., interannual, seasonal, and diurnal variability) is important for studying climate variability, detecting changes in land cover and urban environments, monitoring drought and crop conditions, and indicating wildfire severity [e.g., *Ignatov and Gutman*, 1998, 1999; *Jin and Dickinson*, 2002; *Wan et al.*, 2004; *Braganza et al.*, 2004; *Sun et al.*, 2006a, 2006b; *Weng et al.*, 2004; *Weng*, 2009; *Hansen et al.*, 2010; *Vlassova et al.*, 2014].

Observations of different kinds reveal the spatial and temporal variability of LST from local to global scales for various scientific applications and for evaluating and improving the model performance [e.g., *Reichle et al.*, 2010; *Rodell et al.*, 2004; *Sohrabinia et al.*, 2012]. Currently in the United States, surface sites within the Climate Reference Network (https://www.ncdc.noaa.gov/crn/) and Surface Radiation Network (http://www.esrl.noaa.

gov/gmd/grad/surfrad/) provide long-term frequent observations on a scale of several meters or smaller. Most of the surface sites are sparsely distributed at thermally homogenous locations, and their observations are, in general, associated with small uncertainty [*Becker and Li*, 1995]. Satellites routinely take radiometric LST measurements (interchangeable with the "skin temperature") over broad areas on the scales ranging from hundreds of meters to tens of kilometers. Thermal infrared instruments measure LST on finer resolutions than microwave instruments but are affected by the clouds. Polar-orbiting satellites take day-night observations several times a day (e.g., 4 times/day from Terra and Aqua MODIS) over the globe, and the clear scene observations have been used to derive the diurnal variability of LST with broad geographical coverage [e.g., *Duan et al*., 2014; *Quan et al*., 2014]. Geostationary satellites on higher orbits measure LST over subsets of the world more frequently but on coarser spatial resolution [*Pinker et al*., 2007]. The accuracy of satellite LST retrievals is limited by a number of factors such as the complexity of surface types, sensor performance, and atmospheric correction [*Becker and Li*, 1990; *Dozier and Wan*, 1994; *Li and Becker*, 1993; *Pinker et al*., 2009]. Validating satellite LSTs is still an ongoing research topic, often challenged by the limited ground truth data and their representativeness at satellite pixel scale (in temperature-based method), accuracy of atmospheric radiative transfer model and profiles (in radiation-based method), and accurately matching observations from different instruments in space, time, and viewing angle (in cross-validation method) [*Z. L. Li et al*., 2013]. Typically, the spatial scales and uncertainty of aircraft LST observations fall between the satellite and surface site measurements, varying with atmospheric conditions and the flight altitude. These observations can be intensive during the field campaigns over the selected locations [e.g., *Krishnan et al*., 2015] but have not been often used to investigate the temporal variability of LST over various land cover types.

This study explores the daytime temporal and spatial variability of LST in the Greater Houston area, a region with diverse and rapidly changing land cover types but ground truth LST is lacking. We first show the anomalies of satellite observed LST in September 2013 relative to 2001–2010 (section 3.1). Then, based on daytime aircraft LST collected on the least cloudy day (i.e., 25 September 2013, Figure S1 in the supporting information) during NASA's DISCOVER-AQ (Deriving Information on Surface Conditions from Column and Vertically Resolved Observations Relevant to Air Quality) field campaign period, we formulate daytime LST at multiple locations as a function of time- and location-specific parameters. Using these equations, daytime LST time series is derived at each of these locations and used to evaluate two simulations by the regional-scale community Weather Research and Forecasting (WRF) model [*Skamarock et al*., 2008] with different configurations. The temporal variability of aircraft-derived LSTs is also compared with the observations from a NOAA geostationary satellite and two polar-orbiting satellites to examine their potential to constrain the model. Spatial distributions of LST at late morning and early afternoon hours on this day from both geostationary and polar-orbiting satellites are illustrated and related to the land cover types and vegetation conditions (sections 3.2 and 3.3). Finally, the conclusions and suggestions are given in section 4.

2. Data and Methods

2.1. DISCOVER-AQ Aircraft LST Observations and Diurnal Temperature Cycle Model

NASA's DISCOVER-AQ field experiment is a multiyear campaign beginning in 2011, designed to improve the use of satellites to monitor air quality for public health and environmental benefit [*Crawford et al*., 2014; http://discover-aq.larc.nasa.gov]. Four DISCOVER-AQ deployments were conducted in Washington, DC (July 2011), California (January and Feburary 2013), Texas (September 2013), and Colorado (July and August 2014). During the Texas deployment, airborne observations of meteorological and chemical species were made on NASA's P-3B aircraft on 9 days (Figure S1) at eight selected locations in the Greater Houston area 3 times a day (i.e., morning, noon to early afternoon, and late afternoon) to explore their spatial and diurnal variability. The focused eight locations are denoted in Figure 1. Some of the observations were taken above the water around Smith Point and Galveston. Therefore, in this study we mainly focus on the remaining six inland sites, which are located in three counties (from south to north: Brazoria, Harris, and Montgomery). At each location the aircraft flew circularly around areas within 0.1° latitude/longitude ranges (Table 1). Under clear conditions, surface temperature was measured using a Heitronics nadir-viewing Infrared Radiation Pyrometer Model KT 19.85 (http://airbornescience.nasa.gov/sites/default/files/P-3B%20Experimenter%20Handbook%20548-HDBK-0001.pdf; http://www.heitronics.com/fileadmin/content/Prospekte/KT19_Serie_II_e_Prospectus.pdf; http://nsidc.org/data/docs/daac/icebridge/iakst1b/), and the optics and detector are designed to maximize performance for aircraft applications. This pyrometer has a spectral range of 9.6–11.5 μm, a response time of 0.3 s,

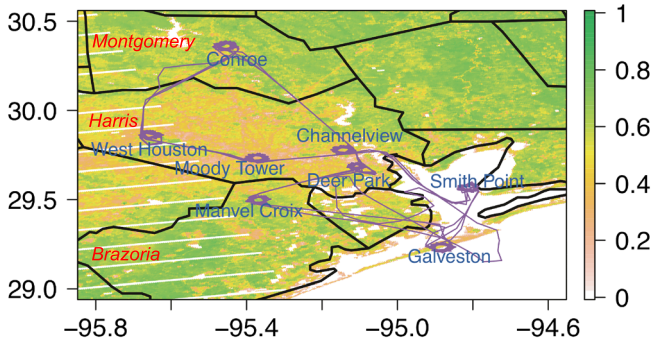

Figure 1. VIIRS NDVI on 25 September 2013 with the P-3B flight track overlaid in purple line and the focused sites labeled in dark blue. Coastal lines and county borders are shown in black lines. The three DISCOVER-AQ focused counties are denoted (red, italic).

an assumed emissivity of 0.97, and a temperature range of −50° to +200°C. The accuracy is ±0.5% plus 0.7% of the difference between target temperature and housing temperature. The pyrometer has a 2° field of view, and for this campaign its footprints ranged from <10 m to tens of meters in radius varying with the flight altitudes. The measurements are achieved in 1 s frequency, and the temporally averaged data in 10 s, 15 s, and 1 min intervals are publicly available.

Inamdar et al. [2008] developed a two-part, semiempirical diurnal temperature cycle model to describe the temporal evolution of LST during the daytime and nighttime separately. *Duan et al.* [2013, 2014] improved this model and derived LST diurnal cycles based on MODIS day-night LST measurements during July 2010 in the Mediterranean region. In this study, the daytime airborne LST measurements at six Houston sites are used to derive LST at other daytimes of this day, and the daytime parts of the equations from *Duan et al.* [2014] were used:

$$T_s^d(t) = T_0 + T_a \cos\left(\frac{\pi}{\omega}(t - t_m)\right),\ t < t_s \tag{1a}$$

$$\omega = \frac{4}{3}(t_m - t_{sr}) \tag{1b}$$

where $T_s^d(t)$, T_0, T_a, t_m, t_{sr}, and t_s represent daytime LST at hour t, the residual temperature, temperature amplitude, time at which LST reaches its daily maximum, the time of sunrise (7:11 A.M local daylight saving time on 25 September, 5 h behind the UTC time), and the starting time of free attenuation, respectively. t_s was set 1 h before the sunset at 7:15 P.M on this day as suggested by *Duan et al.* [2014]. The three P-3B circuit-wide mean T_s^d values at each location were used to derive the three free parameters of T_0, T_a, t_m in equation (1a). T_s^d at other day times on 25 September at each location were then calculated.

2.2. Satellite Land and Cloud Products

Three sets of satellite products illustrate the daytime spatial distributions of LST and cloud conditions on 25 September 2013. They are as follows: Version 3 hourly GOES Surface and Insolation Products (GSIP) on 0.125° horizontal resolution estimated from the GOES-East/West Imager radiance measurements for the Extended Northern Hemisphere scan sector; Level 2 product from the Moderate Resolution Imaging Spectroradiometer (MODIS) instrument on the Terra and Aqua satellites at ~1 km horizontal resolution (collection 5 of MOD/MYD11 and collection 6 of MOD/MYD06 for the LST and cloud products, respectively). During the

Table 1. Free Parameters t_m, T_0, and T_a in Equations (1a) and (1b) at the Six Sites Derived From the Aircraft LST Observations[a]

Location[b]	USGS Land Use[c]	t_m	T_0	T_a	Aircraft Sampled Latitude (°N)/Longitude (°W) Ranges
Manvel Croix (Brazoria)	Dryland Cropland and Pasture (2); Cropland/Grassland Mosaic (5)	14.0	299.33	6.76	29.47–29.54 / 95.34–95.40
Deer Park (Harris)	Dryland Cropland and Pasture (2); Grassland (7)	14.0	300.90	8.61	29.64–29.71 / 95.06–95.13
Moody Tower (Harris)	Urban and Built-up Land (1)	13.9	298.62	12.84	29.70–29.76 / 95.33–95.41
Channelview (Harris)	Dryland Cropland and Pasture (2); Grassland (7)	14.0	296.85	12.02	29.75–29.80 / 95.11–95.18
West Houston (Harris)	Dryland Cropland and Pasture (2)	13.7	295.83	14.81	29.80–29.89 / 95.62–95.69
Conroe (Montgomery)	Evergreen Needleleaf (14)	14.2	296.08	11.18	30.31–30.39 / 95.41–95.49

[a]The latitude/longitude ranges aircraft sampled at each site and the dominant land use type(s) in corresponding WRF grid box(es) are also indicated.
[b]The county that each site is located in is in the parentheses.
[c]Source of USGS land use categories and descriptions: (http://www2.mmm.ucar.edu/wrf/users/docs/user_guide_V3/users_guide_chap3.htm#_Land_Use_and).

Table 2. Configurations of the WRF 3.6.1 Simulations and References

WRF Case/Configurations	Noah	PX
Domain and resolution	12 km over the continental U.S. (471 × 311 grids), i.e., domain of NOAA's air quality forecasting system	
Initialization	12 km North American Mesoscale Model, which used the Noah land surface model	
Cloud scheme	Kain and Fritsch scheme [*Kain*, 2004]	
Radiation scheme	Rapid Radiative Transfer Model scheme short- and long-wave radiation [*Iacono et al*., 2008]	
Microphysics	New Thompson Scheme [*Thompson et al*., 2008]	
PBL scheme	Yonsei University scheme [*Hong et al*. 2006]	Asymmetric Convective Model version 2 [*Pleim*, 2007]
Surface layer	Monin-Obukhov scheme [*Monin and Obukhov*, 1954]	Pleim-Xiu [*Pleim*, 2006]
Land surface model	Noah [*Chen and Dudhia*, 2001]	Pleim-Xiu [*Xiu and Pleim*, 2001; *Pleim and Xiu*, 2003]
Nudging	Three-dimensional grid nudging for wind, temperature and moisture. PBL nudging was applied only to the wind (U; V)	Three-dimensional grid nudging for wind, temperature and moisture above the PBL, surface and Pleim-Xiu soil nudging [*Pleim and Gilliam*, 2009]

daytime, the Terra and Aqua satellites have late morning and early afternoon overpassing times, respectively; and Level 2 LST and the cloud confidence indicator in the early afternoon from the Environmental Data Records product of the Visible Infrared Imaging Radiometer Suite (VIIRS) instrument on the Suomi-National Polar-orbiting Partnership (S-NPP) satellite at ~750 km horizontal resolution. Previous studies reported larger discrepancies between GOES and MODIS LST during the daytime than the nighttime [*Sun et al*., 2015], affected by viewing geometry and surface conditions. *Li et al*. [2014] evaluated Aqua MODIS LST during 2002–2011 with ground observations at six remote sites in the United States and reported an overall −0.93°K of bias, but the data quality varied significantly by site, time of the day, and season (i.e., positive biases in warm seasons). LSTs from VIIRS and MODIS were evaluated against ground observations at four sites in an arid area of Northwest China, in which VIIRS demonstrated satisfactory quality, and MODIS daytime LSTs showed negative biases [*H. Li et al*., 2013]. Studies that intercompare LSTs from all these instruments are still needed.

Additionally, the VIIRS top-of-atmosphere normalized difference vegetation index (NDVI) and top-of-canopy enhanced vegetation index (EVI) measurements on this day were also used as dynamical land indicators and to help interpret the LST spatial distributions. NDVI is the most commonly used vegetation index, calculated using the reflected visible and near-infrared light on vegetation. EVI is more sensitive to the differences in heavily vegetated areas. VIIRS vegetation indexes, in general, compare well with those derived from the Aqua MODIS [*Hook et al*., 2012]. Vegetation indexes and LST have been used as drought indicators and found to be anticorrelated during warm seasons due to vegetation's cooling effects [e.g., *Sun and Kafatos*, 2007; *Karnieli et al*., 2010].

2.3. WRF Model Simulations

The surface skin temperatures from two simulations (cases "Noah" and "PX") using the WRF model version 3.6.1 (released in August 2014) on 25 September were used to interpret the LST diurnal variability at the six Houston sites. The different results from these simulations help assess the impact of land surface model (LSM) and nudging choices on the modeled LST. Both simulations were conducted on a $12 \times 12\ km^2$ horizontal resolution grid over the continental U.S. (i.e., the domain of NOAA's air quality forecasting system), from 1 September 2013, at 00Z, to 1 October 2013, at 12Z. The simulations were restarted every 5 days with a 12 h overlap between each segment and were saved hourly. Key physics options and corresponding references of the WRF simulations are summarized in Table 2. The configurations of case Noah were suggested by the Texas Commission on Environmental Quality (TCEQ). Particularly, the 4-layer (with thickness of 10, 30, 60, and 100 cm) Noah LSM [*Chen and Dudhia*, 2001] was used, and only three-dimensional grid nudging was implemented for temperature, moisture, and winds. In case PX, the 2-layer (a 1 cm surface layer and a 99 cm root zone layer) Pleim-Xiu LSM [*Xiu and Pleim*, 2001; *Pleim and Xiu*, 2003] and the surface/indirect soil nudging [*Pleim and Gilliam*, 2009; *Gilliam and Pleim*, 2010] were activated (as recommended in the WRF Users'

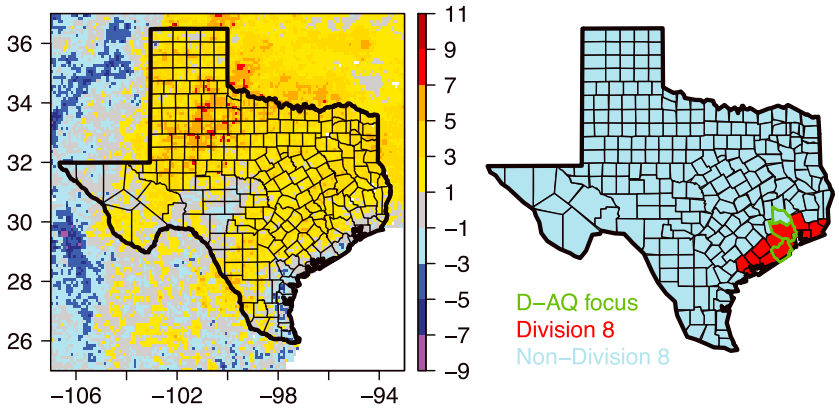

Figure 2. (left) The anomalies of LST in°K in September 2013 over Texas based on daytime Terra LST observations. The anomalies are related to the average values in Septembers during 2001–2010. Data used in the plot (in 0.1° × 0.1° resolution) were from the NASA Earth Observations at http://neo.sci.gsfc.nasa.gov/view.php?datasetId=MOD_LSTAD_M&year=2013. (right) Definition of NOAA climate division 8 (red) and nondivision 8 regions in Texas (light blue) and the DISCOVER-AQ focused counties (green). The NOAA climate divisions are defined at http://www.ncdc.noaa.gov/monitoring-references/maps/us-climate-divisions.php. The palmer drought severity index in the climate division 8 is introduced in section 3.1.

Guide) and informed by the National Centers for Environmental Prediction Automated Data Processing Global Surface Observational Weather Data (i.e., ds461, http://rda.ucar.edu/datasets/ds461.0/). The Noah and PX LSM use grid-dominant and fractional land use types, respectively. *Miao et al*. [2007] reported evident differences in simulated near-surface air temperature in Sweden by using Noah and PX LSMs. Simulations over Texas using WRF version 3.2 in summer 2006 indicated that the configurations similar to our PX case resulted in better WRF performance on 2 m temperature and wind than the Noah case [*Byun et al*., 2011].

3. Results and Discussion

3.1. The LST Anomalies in September 2013 Compared to the Past Decade Averages

Satellites provide long-term LST observations, which are often used to indicate the drought conditions. Figure 2 shows that the MODIS-observed daytime LSTs in this September in the southeastern Texas differed from the mean values during 2001–2010 by $<$5°K, with negative anomalies in several coastal counties and positive anomalies in most inland counties. The mean LST anomaly of ~0.70°K over the Texas climate division 8 indicates hotter and drier conditions in this month than in the Septembers during 2001–2010. This is consistent with the finding from the monthly Palmer Drought Severity Index (PDSI) [*Palmer*, 1965; *Alley*, 1984; http://www.ncdc.noaa.gov/temp-and-precip/drought/historical-palmers.php], a widely used index for identifying long-term and abnormal moisture deficiency or excess: the monthly PDSI of −2.7 (moderate drought) in this September is smaller than the mean PDSI value (0.328) of the Septembers during 2001–2010. Overall, the three DISCOVER-AQ focused counties (Brazoria, Harris, and Montgomery) showed a drier-than-division-average condition, as indicated from its mean LST anomaly of ~0.88°K.

3.2. Spatial and Temporal Variability of Aircraft-Derived LST in Houston

The P-3B aircraft sampled over areas of diverse land use types in Houston during DISCOVER-AQ, as indicated by the US Geological Survey (USGS) land use categories used in the WRF simulations (Table 1). The six inland sites include urban (Moody Tower, in the city center), cropland/grassland (West Houston, Channelview, Deer Park, and Manvel Croix), and forest (Conroe, farthest from the city center). Figures 1 and S2 show that the VIIRS vegetation conditions varied among these sites on this day, ranging from $<$0.4 (in urban) to ~0.7 (in the forest) for NDVI and $<$0.2 (in urban) to 0.3–0.6 (in the forest) for EVI. On smaller spatial scales, i.e., at each of the six sites, the vegetation indexes around/within the spirals were also highly variable.

At each site, the highest LSTs were observed on P-3B at its second circuit near 1300–1400 local time. Large variability in LSTs was also seen at each circuit, with spreads of $>$40°K (based on ~700–900 data points) at some circuits from the achieved 1 s data set and ~10°K from the 1 min averaged aircraft observation data set (open dots in Figure 3). These reflect the mixing surface conditions the aircraft sampled above. The 1 min averaged aircraft

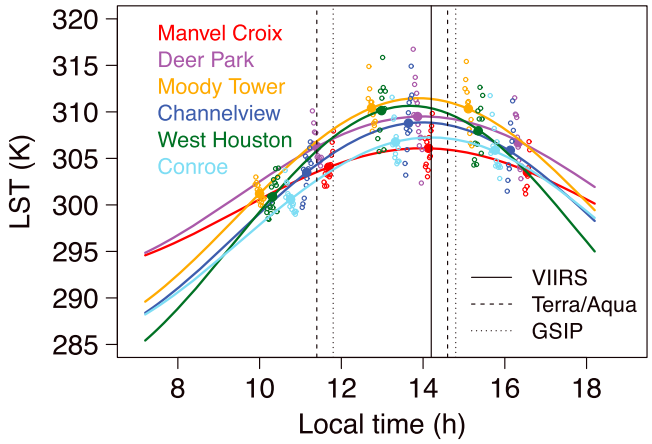

Figure 3. Time series of LST from P-3B at six inland locations in the Greater Houston area on 25 September 2013. Open circles are 1 min averaged observations (details in section 3.2), and the filled dots indicate the circuit-mean values. LSTs derived by equations (1a) and (1b) are in solid lines. Satellite overpassing times (for plots in the lower panels in Figures 4 and 5) are indicated in black vertical lines.

observations were shown in Figure 3 for better readability. Figure S3 compares the time series of LSTs from both the 1 s and the 1 min averaged data sets, and the mean values of LSTs at each circuit from both data sets are almost identical. Water vapor amount on clear-sky days is generally smaller than under all-sky conditions. Its interference on these measurements is assumed to be smaller than the standard deviation of the samples at each circuit (e.g., for the 1 min averaged data, ranging from <1°K to 4°K depending on the location and the time of day), which is defined as the representation errors and will be accounted for when evaluating the WRF model. We calculated three circuit-wide mean LSTs for each site, based on which the three free parameters in equations (1a) and (1b) were determined (Table 1). The time series of daytime LST at the six sites were then derived using the diurnal LST model and these aircraft-derived parameters. At most sites, the LST values reached their daily maxima at near 1400 local time (i.e., t_m in Table 1), close to the overpassing times of the Aqua and S-NPP satellites on this day. In the early afternoon, the LSTs at locations with smaller vegetation indexes near the city center (Moody Tower, Deer Park, West Houston, and Channelview) were higher than those at the other two sites Conroe and Manvel Croix, where, in general, more vegetation was observed. Table 3 indicates negative correlations between the aircraft-derived LSTs near the VIIRS overpassing times and the collocated VIIRS vegetation index values at the six sites. These results are consistent with the findings by *Peng et al.* [2012, and the references therein] that daytime surface urban heat island (i.e., the LST differences between the urban and suburban areas) are negatively correlated with the vegetation cover in hundreds of big cities worldwide.

The pyrometer's constant emissivity setting of 0.97 may not be realistic for all studied locations on this day. Emissivity varies among different surface types, and it differs in space and time: e.g., emissivity values smaller than 0.97 present at urban environment, where more energy is absorbed by land. Over vegetated regions, emissivity depends on the vegetation type and density, as well as its state of growth. There are still great challenges to accurately determine emissivity values [e.g., *Jin and Liang*, 2006; *Tao et al.*, 2013, and the references therein]. Unrealistic emissivity can introduce biases to the aircraft-derived LSTs, but we expect these biases to be smaller than its discrepancies from the satellite and modeling data sets, which will be shown in section 3.3. This impact is suggested to be carefully quantified in future studies.

Across the inland Houston domain, anticorrelation (listed in Table 3) is also found between the VIIRS vegetation indexes (Figures 1 and S2) and LST (Figure 4, bottom, right panel). Higher LSTs (>315°K) were observed by VIIRS near and around the city center than in the rural/suburban areas. Similar spatial distributions of LST

Table 3. The Correlation Coefficients Between LST and the VIIRS Vegetation Indexes

LST Data	Number of VI/LST Data Points	VIIRS EVI	VIIRS NDVI
Aircraft-derived, at the six locations[a]	6	−0.87	−0.89
VIIRS, at the six locations[a]	6	−0.78	−0.92
VIIRS, inland Houston (29.4–30.5°N; 95–95.8°W, gridded to 0.1° × 0.1°)	88	−0.67	−0.84

[a]Locations defined in Table 1.

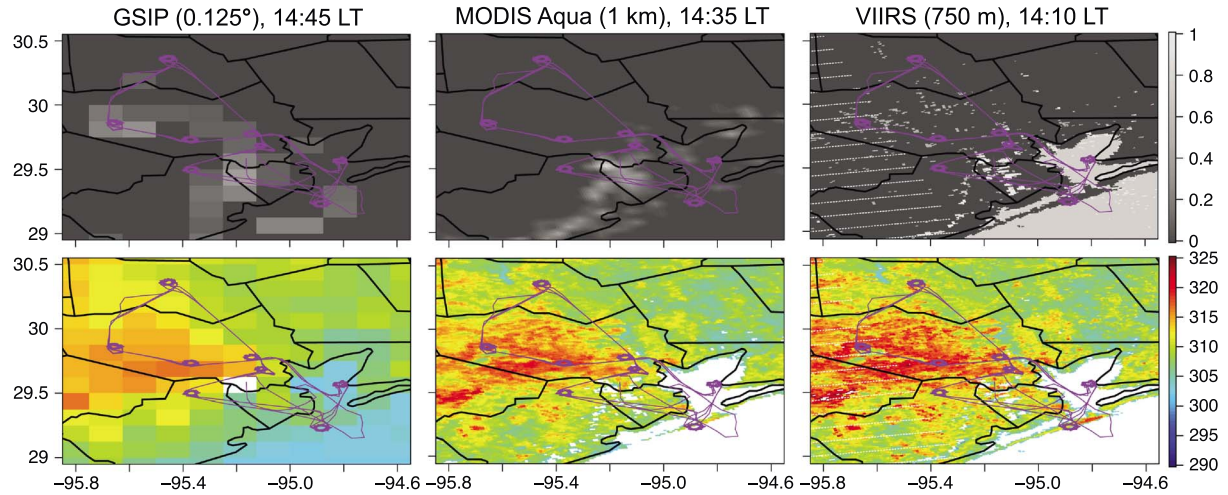

Figure 4. (top) Spatial distributions of cloud fraction and (bottom) LST in°K in the early afternoon on 25 September 2013, from (left) GSIP, (middle) MODIS Aqua, and (right) VIIRS. For top right panel plot, VIIRS cloud confidence indicator of "Confidently Clear", "Probably Clear", "Probably Cloudy", and "Confidently Cloudy" are assigned cloud fraction values of 0, 0.5, 0.75, and 1, respectively, and LST values under Confidently Cloudy conditions are unavailable (for the bottom right panel plot). P-3B flight track on this day is overlaid in purple line.

over the Houston area were also observed by the GOES and Aqua MODIS in the early afternoon (between 1400 and 1500 local time on this day when clear scenes dominated the domain at their overpassing times) (Figure 4). The LSTs observed by GOES and MODIS in the late morning in Houston are >10°K lower than in the early afternoon, with similar spatial patterns, but the GSIP product indicates approximately 3–5°K higher LST than the Terra MODIS. In some areas east to Houston, the differences between GSIP and Terra MODIS are larger than 5°K (Figure 5). Due to their finer horizontal resolutions, the MODIS and VIIRS LST products offer greater local details than GSIP. In general, the different sensor characteristics, sampling strategies, and retrieval algorithms are the main reasons for the differences among these products.

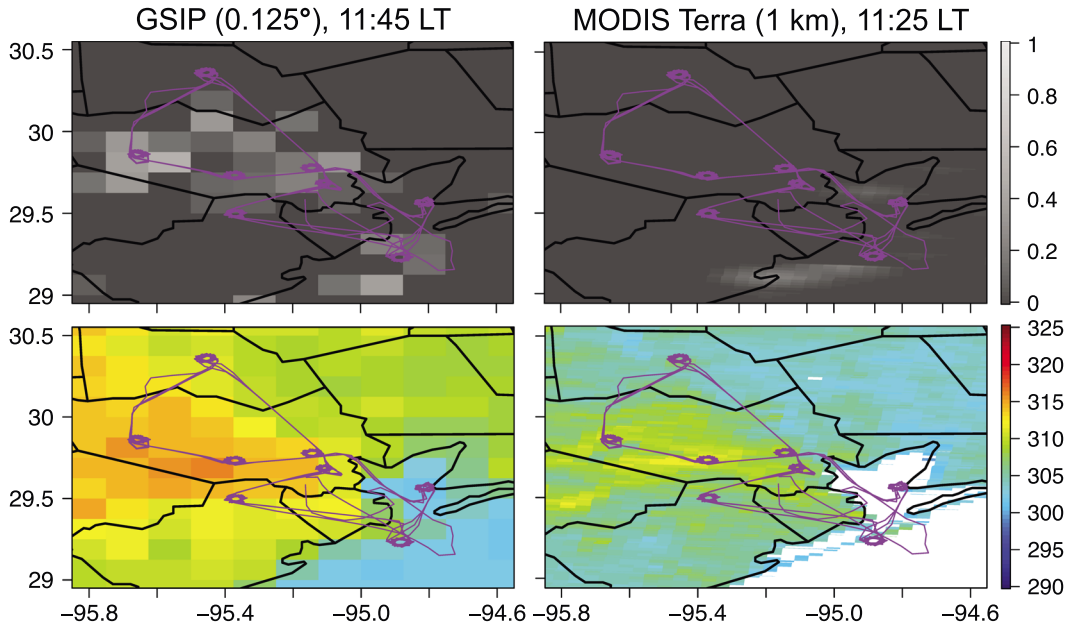

Figure 5. Spatial distributions of (upper) cloud fraction and (lower) LST in°K in the late morning on 25 September 2013, from (left) GSIP and (right) MODIS Terra. P-3B flight track on this day is overlaid in purple line.

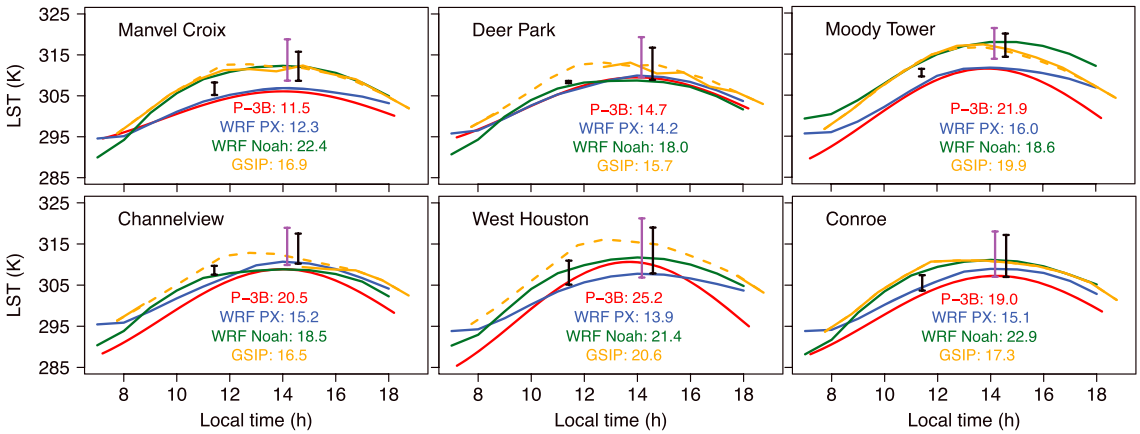

Figure 6. Aircraft-derived, GSIP, and WRF modeled daytime LST time series at six locations in Houston on 25 September 2013. Differences between maximum and minimum LST values are shown for each data set. GSIP data at all scenes and clear scenes (GSIP cloud fraction = 0) are shown in solid and dash lines, respectively. The range of LSTs observed by MODIS (Terra and Aqua) and VIIRS at each location are overlaid in black and purple vertical bars, respectively.

3.3. Comparing Aircraft-Derived LST With WRF-Simulated and Satellite LST

The aircraft-derived temporal evolution of daytime LST at each site was compared with the two WRF simulations. To extract the modeled LST values corresponding to the aircraft observations, we first projected the aircraft sampling locations to the model space. At each site these aircraft observations fell into 1–4 model grids, indicating the aircraft spirals are on comparable spatial scales to the model. Then the LST values at each hour of the day were averaged over all model grids that the samples fell into to create the modeled LST time series in Figure 6. The discrepancies between aircraft and modeled LSTs are often larger than the representation errors of LST. Largest aircraft-derived $Diff_{LST}$ (i.e., the differences between the maximum and minimum LSTs throughout the daytime) occurred in West Houston, followed by Moody Tower and Channelview, where the $Diff_{LST}$ values were underpredicted in both WRF simulations. The smallest $Diff_{LST}$ value was found at Manvel Croix, which was overpredicted in both WRF simulations. Smaller $Diff_{LST}$ values are shown at all six sites in case PX than in case Noah. Note that the starting and ending times in Figure 6 are slightly different dependent on the format of each data set (i.e., the WRF results were recorded at 00 min of each hour; GSIP data are provided at 45 min of each hour; aircraft-derived data started from the time of sunrise and ended at 1 h before the sunset), but the influences would not change the above conclusions from the comparisons. Unlike case Noah that provides true skin temperature, the fact that top ground temperature in case PX is used to approximate to LST for this comparison, can lead to a slightly different $Diff_{LST}$ than the LST measurements made to a much thinner depth of the ground. Ongoing work includes adding diagnostic skin temperature to the PX scheme.

Using the aircraft-derived LSTs as the reference line, the time-dependent root-mean-square errors (RMSE) from the two WRF simulations are summarized in Table 4. The WRF performance on LST varies among the sites and the time of day, and neither case shows significant better performance on any land type (in WRF

Table 4. Evaluation of WRF Modeled LST With the Aircraft-Derived LST at Six Sites Within Different Time Intervals on 25 September 2013[a]

WRF case	Local time (hh:mm)	Manvel Croix	Deer Park	Moody Tower	Channelview	West Houston	Conroe
Noah	08:00–11:00	4.34	1.62	6.99	4.00	4.37	4.64
	12:00–15:00	6.28	0.64	6.58	0.94	1.70	4.35
	16:00–18:00	5.30	0.56	10.45	2.64	6.74	5.03
	08:00–18:00	5.37	1.09	7.96	2.83	4.52	4.65
PX	08:00–11:00	0.68	1.74	2.52	2.66	2.81	1.93
	12:00–15:00	0.77	3.42	5.53	4.07	1.55	2.59
	16:00–18:00	2.02	3.55	6.10	3.97	2.60	3.02
	08:00–18:00	1.23	2.96	4.85	3.59	2.36	2.51

[a]Root-mean-square errors (°K) are listed.

definition) over the others. The best WRF performance was found at Deer Park and Manvel Croix in case Noah and PX, respectively. Throughout the daytime (8–18 local time) and at the afternoon hours (12–15; 16–18 local time), case PX shows better performance than case Noah except at Channelview and Dear Park. During the morning time, case Noah performed slightly better only at Deer Park.

GSIP LSTs during the daytime at each site were extracted similarly, for all scenes (dashed lines) and only the cloud-free scene (i.e., where the GSIP cloud fraction equals to 0 such as the dark grey areas in upper left panels of Figures 4 and 5, solid lines). Although GSIP is often higher than the aircraft-derived LST and is subject to cloud contamination, it provides useful information of the LST temporal variability missing from the polar-orbiting satellite products. However, in this study GSIP LST does not show notably better match with the aircraft-derived LSTs than the presented WRF simulations, in terms of RMSEs and the performance in $Diff_{LST}$. To be able to integrate this product into models, careful data filtering and appropriate bias correction should be applied, and meanwhile, continuous improvement on the GOES LST products should be made.

Tens of MODIS and VIIRS pixels are collocated with (i.e., the data that fell within the corresponding aircraft spiral's latitude/longitude ranges listed in Table 1) at each of six aircraft-sampled locations, and the ranges of LST observed by these two satellites in these pixels are shown as vertical bars in Figure 6. At all locations, wider LST ranges (5.7–14.4°K) were observed in the early afternoon than in the late morning (0.5–5.8°K), and the widest LST ranges were observed by MODIS Terra and Aqua in West Houston. In the early afternoon, VIIRS observed wider LST ranges than Aqua MODIS due to its finer spatial resolution. This again reflects the impact of diverse surface conditions at these locations and the importance of finer satellite resolution to detecting local details. Consistent with the findings from Figures 4 and 5, GSIP LSTs in the early afternoon hours fell into the ranges of Aqua MODIS and VIIRS but were up to ~5°K higher than Terra MODIS in the late morning. The LSTs derived from the aircraft and in the WRF case PX are often near the lower ends of those from VIIRS and MODIS. The location- and time-varying discrepancies among the satellite- and aircraft-derived LSTs indicate that large uncertainties exist for LSTs sampled on these different platforms over smaller temporal and spatial scales. Therefore, great challenges are posed for the evaluation of regional-scale model simulated LSTs, especially in the areas of diverse surface types and lacking surface site observations such as in Houston.

4. Conclusions and Suggestions

We derived daytime time series of LST at six locations in the Greater Houston area on the least cloudy day during the DISCOVER-AQ Houston deployment using aircraft observations and a semiempirical diurnal temperature cycle model. The intense aircraft data were demonstrated useful for informing us the LST temporal variability on local to regional scales, in addition to the existing geostationary and polar-orbiting satellite observations. This method can be broadly applied to other locations and times, such as during the remaining three DISCOVER-AQ deployments in populated regions of diverse land uses (i.e., Washington D.C., California, and Colorado) for better understanding the conditions there.

We also explored the usefulness of aircraft data for evaluating satellite and modeled LSTs in Houston. Compared with the aircraft-derived LSTs, two WRF simulations that were configured differently showed variable performance on LST's daytime temporal variability at the six locations. Accurately modeling LST is still challenging, but alternative configurations in WRF should be experimented, with complete assessment of other simulated surface/near-surface meteorological variables. Incorporating well-evaluated observations from aircraft (manned and unmanned) and satellites into the model can be beneficial but is still challenged by the large uncertainties in the LSTs sampled on the various platforms, especially over small temporal and spatial scales in regions of complex surface conditions. Increasing the number of surface sites and carrying out well-designed aircraft campaigns in the future will be helpful for evaluating the used semiempirical diurnal temperature cycle model (e.g., taking observations at the targeted location for more than 3 times a day), as well as the remote sensing products and model simulations. In addition, suitable methods of merging LSTs from the geostationary (frequent sampling) and polar-orbiting satellites (finer spatial resolution) would be encouraged, so that the advantages of both kinds of the products could be combined.

We also showed that LSTs from aircraft and satellites in the early afternoon were anticorrelated with satellite vegetation indexes on this day. This emphasized the importance of vegetation cover in urban planning due to its cooling effect and further impact on biogenic emissions and the regional air quality, which are sensitive to temperature and radiation.

Acknowledgments
We thank the contributions from Y. Wu, K. Doty (U Alabama), and P. Winter (Wintronics). The views, opinions, and findings contained in this paper are those of the author(s) and should not be construed as an official National Oceanic and Atmospheric Administration or U.S. Government position, policy, or decision.The preparation of this paper was financed through a grant from the Texas Commission on Environmental Quality (TCEQ), administered by The University of Texas through the Air Quality Research Program. The contents, findings, opinions, and conclusions are the work of the author(s) and do not necessarily represent the findings, opinions, or conclusions of the TCEQ.The open access to the used aircraft and satellite data is acknowledged: DISCOVER-AQ P-3B (http://www-air.larc.nasa.gov/cgi-bin/ArcView/discover-aq.tx-2013), doi: 10.5067/Aircraft/DISCOVER-AQ/Aerosol-TraceGas; GSIP (http://www.class.ngdc.noaa.gov/saa/products/search?datatype_family=GSIP); MODIS (https://ladsweb.nascom.nasa.gov/data/); VIIRS (http://www.class.ngdc.noaa.gov/saa/products/search?sub_id=0&datatype_family=VIIRS_EDR&-submit.x=17&submit.y=9). The WRF model output can be made available upon request.

References

Alley, W. M. (1984), The Palmer drought severity index: Limitation and Assumptions, *J. Climate Appl. Meteorol.*, *23*, 1100–1109.
Becker, F., and Z.-L. Li (1990), Towards a local split window method over land surfaces, *Remote Sens.*, *11*, 369–393, doi:10.1080/01431169008955028.
Becker, F., and Z.-L. Li (1995), Surface temperature and emissivity at various scales: Definition, measurement and related problems, *Remote Sens. Rev.*, *12*, 225–253, doi:10.1080/02757259509532286.
Braganza, K., D. J. Karoly, and J. M. Arblaster (2004), Diurnal temperature range as an index of global climate change during the twentieth century, *Geophys. Res. Lett.*, *31*, L13217, doi:10.1029/2004GL019998.
Byun, D., et al. (2011), Final report: Improvement of meteorological modeling by accurate prediction of soil moisture in the Weather Research and Forecasting (WRF) Model. [Available at https://www.tceq.texas.gov/assets/public/implementation/air/am/contracts/reports/mm/582886246FY1009-NOAA_WRF_Soil_Moisture_20110331.pdf reported by NOAA ARL to Texas Commission on Environmental Quality.]
Chen, F., and J. Dudhia (2001), Coupling an advanced land surface-hydrology model with the Penn State-NCAR MM5 modeling system. Part I: Model implementation and sensitivity, *Mon. Weather Rev.*, *129*, 569–585, doi:10.1175/1520-0493(2001)129<0569:CAALSH>2.0.CO;2.
Crawford, J. H., R. R. Dickerson, and J. C. Hains (2014), DISCOVER-AQ: Observations and early results, *Environ. Manage.*, *September 2014*, 8–15.
Dozier, J., and Z. Wan (1994), Development of practical multiband algorithms for estimating land-surface temperature from EOS/MODIS data, *Adv. Space Res.*, *14*(3), 81–90, doi:10.1016/0273-1177(94)90196-1.
Duan, S.-B., Z.-L. Li, H. Wu, B.-H. Tang, X. Jiang, and G. Zhou (2013), Modeling of day-to-day temporal progression of clear-sky land surface temperature, *IEEE Geosci. Remote Sens. Lett.*, *10*, 1050–1054, doi:10.1109/LGRS.2012.2228465.
Duan, S.-B., Z.-L. Li, B.-H. Tang, H. Wu, R. Tang, Y. Bi, and G. Zhou (2014), Estimation of diurnal cycle of land surface temperature at high temporal and spatial resolution from clear-sky MODIS data, *Remote Sens.*, *6*, 3247–3262, doi:10.3390/rs6043247.
Gilliam, R. C., and J. E. Pleim (2010), Performance assessment of new land surface and planetary boundary layer physics in the WRF-ARW, *J. Appl. Meteorol. Climatol.*, *49*, 760–774, doi:10.1175/2009JAMC2126.1.
Hansen, J., R. Ruedy, M. Sato, and K. Lo (2010), Global surface temperature change, *Rev. Geophys.*, *48*, RG4004, doi:10.1029/2010RG000345.
Hong, S.-Y., Y. Noh, and J. Dudhia (2006), A new vertical diffusion package with an explicit treatment of entrainment processes, *Mon. Weather Rev.*, *134*, 2318–2341, doi:10.1175/MWR3199.1.
Hook, S., et al. (2012), An evaluation of the Suomi-NPP Visible Infrared Imaging Radiometer Suite (VIIRS) and the associated environmental data records for land science after early evaluation on on-orbit performance. [Available at http://npp.gsfc.nasa.gov/DEW_NPP_reports/VIIRS%20Land%20Products%20Report%20 (Dec-19-2012).pdf.]
Iacono, M. J., J. S. Delamere, E. J. Mlawer, M. W. Shephard, S. A. Clough, and W. D. Collins (2008), Radiative forcing by long-lived greenhouse gases: Calculations with the AER radiative transfer models, *J. Geophys. Res.*, *113*, D13103, doi:10.1029/2008JD009944.
Ignatov, A., and G. Gutman (1998), Diurnal cycles of land surface temperatures, *Adv. Space Res.*, *22*(5), 641–644, doi:10.1016/S0273-1177(97)01125-3.
Ignatov, A., and G. Gutman (1999), Monthly mean diurnal cycles in surface temperatures over land for global climate studies, *J. Clim.*, *12*, 1900–1910, doi:10.1175/1520-0442(1999)012<1900:MMDCIS>2.0.CO;2.
Inamdar, A. K., A. French, S. Hook, G. Vaughan, and W. Luckett (2008), Land surface temperature retrieval at high spatial and temporal resolutions over the southwestern United States, *J. Geophys. Res.*, *113*, D07107, doi:10.1029/2007JD009048.
Jin, M., and R. E. Dickinson (2002), New observational evidence for global warming from satellite, *Geophys. Res. Lett.*, *29*(10), 1400, doi:10.1029/2001GL013833.
Jin, M., and R. E. Dickinson (2010), Land surface skin temperature climatology: Benefitting from the strengths of satellite observations, *Environ. Res. Lett.*, *5*, 044004, doi:10.1088/1748-9326/5/4/044004.
Jin, M., and S. Liang (2006), An improved land surface emissivity parameter for land surface models using global remote sensing observations, *J. Clim.*, *19*, 2867–2881, doi:10.1175/JCLI3720.1.
Kain, J. S. (2004), The Kain-Fritsch convective parameterization: An update, *J. Appl. Meteorol.*, *43*, 170–181, doi:10.1175/1520-0450(2004)043<0170:TKCPAU>2.0.CO;2.
Karnieli, A., N. Agam, R. T. Pinker, M. Anderson, M. L. Imhoff, and G. G. Gutman (2010), Use of NDVI and land surface temperature for drought assessment: Merits and limitations, *J. Clim.*, *23*, 618–633, doi:10.1175/2009JCLI2900.1.
Krishnan, P., J. Kochendorfer, E. J. Dumas, P. C. Guillevic, C. B. Baker, T. P. Meyers, and B. Martos (2015), Comparison of in-situ, aircraft, and satellite land surface temperature measurements over a NOAA Climate Reference Network site, *Remote Sens. Environ.*, *165*, 249–264, doi:10.1016/j.rse.2015.05.011.
Li, H., D. Sun, Y. Yu, H. Wang, Y. Liu, Q. Liu, Y. Du, H. Wang, and B. Cao (2013), Evaluation of the VIIRS and MODIS LST products in an arid area of Northwest China, *Remote Sens. Environ.*, *142*, 111–121, doi:10.1016/j.rse.2013.11.014.
Li, S., Y. Yu, D. Sun, D. Tarpley, X. Zhan, and L. Chiu (2014), Evaluation of 10 year AQUA/MODIS land surface temperature with SURFRAD observations, *Int. J. Remote Sens.*, *35*(3), 830–856, doi:10.1080/01431161.2013.873149.
Li, Z. L., and F. Becker (1993), Feasibility of land surface temperature and emissivity determination from AVHRR data, *Remote Sens. Environ.*, *43*, 67–85, doi:10.1016/0034-4257(93)90065-6.
Li, Z. L., B.-H. Tang, H. Wu, H. Ren, G. Yan, Z. Wan, I. F. Trigo, and J. A. Sobrino (2013), Satellite-derived land surface temperature: Current status and perspectives, *Remote Sens. Environ.*, *131*, 14–37, doi:10.1016/j.rse.2012.12.008.
Mannstein, H. (1987), Surface energy budget, surface temperature and thermal inertia, in *Remote Sens. Applications In Meteorology and Climatology*, *ASI Ser.*, vol. 201, pp. 391–410, NATO, Dordrecht, Netherlands.
Miao, J.-F., D. Chen, and K. Borne (2007), Evaluation and comparison of Noah and Pleim–Xiu land surface models in MM5 using GÖTE2001 data: Spatial and temporal variations in near-surface air temperature, *J. Appl. Meteorol. Climatol.*, *46*, 1587–1605, doi:10.1175/JAM2561.1.
Monin, A. S., and A. M. Obukhov (1954), Basic laws of turbulent mixing in the surface layer of the atmosphere, *Tr. Akad. Nauk. SSSR Geophiz. Inst.*, *24*(151), 163–187.
Palmer, W. C. (1965), *Meteorological Drought*, *Res. Paper*, vol. 45, 58 pp., Dep. of Commerce, Washington, D. C.
Peng, S., S. Piao, P. Ciais, P. Friedlingstein, C. Ottle, F. Breon, H. Nan, L. Zhou, and R. Myneni (2012), Surface urban heat island across 419 global big cities, *Environ. Sci. Technol.*, *46*, 696–703, doi:10.1021/es2030438.
Pinker, R. T., D. Sun, M. Miller, and G. J. Robinson (2007), Diurnal cycle of land surface temperature in a desert encroachment zone as observed from satellites, *Geophys. Res. Lett.*, *34*, L11809, doi:10.1029/2007GL030186.
Pinker, R. T., D. Sun, M.-P. Hung, C. Li, and J. B. Basara (2009), Evaluation of satellite estimates of land surface temperature from GOES over the United States, *J. Appl. Meteorol. Climatol.*, *48*, 167–180, doi:10.1175/2008JAMC1781.1.
Pleim, J. (2007), A combined local and nonlocal closure model for the atmospheric 548 boundary layer, Part I: Model description and testing, *J. Appl. Meteorol. Climatol.*, *46*, 1383–1395, doi:10.1175/JAM2539.1.

Pleim, J. E. (2006), A simple, efficient solution of flux–profile relationships in the atmospheric surface layer, *J. Appl. Meteorol. Climatol.*, *45*, 341–347, doi:10.1175/JAM2339.1.

Pleim, J. E., and R. Gilliam (2009), An indirect data assimilation scheme for deep soil temperature in the Pleim-Xiu land surface model, *J. Appl. Meteorol. Climatol.*, *48*, 1362–1376, doi:10.1175/2009JAMC2053.1.

Pleim, J. E., and A. Xiu (2003), Development of a land surface model. Part II: Data assimilation, *J. Appl. Meteorol.*, *42*, 1811–1822, doi:10.1175/1520-0450(2003)042<1811:DOALSM>2.0.CO;2.

Quan, J., Y. Chen, W. Zhan, J. Wang, J. Voogt, and J. Li (2014), A hybrid method combining neighborhood information from satellite data with modeled diurnal temperature cycles over consecutive days, *Remote Sens. Environ.*, *155*, 257–274, doi:10.1016/j.rse.2014.08.034.

Reichle, R. H., S. V. Kumar, S. P. Mahanama, R. D. Koster, and Q. Liu (2010), Assimilation of satellite-derived skin temperature observations into land surface models, *J. Hydrometeorol.*, *11*, 1103–1122, doi:10.1175/2010JHM1262.1.

Rodell, M., et al. (2004), The global land data assimilation system, *Bull. Am. Meteorol. Soc.*, *85*, 381–394, doi:10.1175/BAMS-85-3-381.

Skamarock, W., J. B. Klemp, J. Dudhia, D. O. Gill, D. Barker, M. G. Duda, X.-Y. Huang, and W. Wang (2008), A description of the advanced research WRF version 3, *NCAR Tech. Note NCAR/TN-475 + STR*, doi:10.5065/D68S4MVH.

Sohrabinia, M., W. Rack, and P. Zawar-Reza (2012), Analysis of MODIS LST Compared with WRF Model and in situ Data over the Waimakariri River Basin, Canterbury, New Zealand, *Remote Sens.*, *4*, 3501–3527, doi:10.3390/rs4113501.

Sun, D., and M. Kafatos (2007), Note on the NDVI-LST relationship and the use of temperature-related drought indices over North America, *Geophys. Res. Lett.*, *34*, L24406, doi:10.1029/2007GL031485.

Sun, D., M. Kafatos, R. Pinker, and D. Easterling (2006a), Comparison of seasonal variations in diurnal temperature range as observed from satellites and surface observations, *IEEE Trans. Geosci. Remote Sens.*, *44*(10), 2779–2785, doi:10.1109/TGRS.2006.871895.

Sun, D., Y. Yu, H. Yang, L. Fang, Q. Liu, and J. Shi (2015), A case study for intercomparison of land surface temperature retrieved from GOES and MODIS, *Int. J. Digital Earth*, *8*(6), 476–494, doi:10.1080/17538947.2014.906509.

Sun, D. L., R. Pinker, and M. Kafatos (2006b), Diurnal temperature range over the United States: A satellite view, *Geophys. Res. Lett.*, *33*, L05705, doi:10.1029/2005GL024780.

Tao, Z., J. A. Santanello, M. Chin, S. Zhou, Q. Tan, E. M. Kemp, and C. D. Peters-Lidard (2013), Effect of land cover on atmospheric processes and air quality over the continental United States—A NASA Unified WRF (NU-WRF) model study, *Atmos. Chem. Phys.*, *13*, 6207–6226, doi:10.5194/acp-13-6207-2013.

Thompson, G., P. R. Field, R. M. Rasmussen, and W. D. Hall (2008), Explicit forecasts of winter precipitation using an improved bulk microphysics scheme, Part II: Implementation of a new snow parameterization, *Mon. Weather Rev.*, *136*, 5095–5115, doi:10.1175/2008MWR2387.1.

Vinnikov, K. Y., Y. Yu, M. K. Rama Varma Raja, D. Tarpley, and M. D. Goldberg (2008), Diurnal-seasonal and weather-related variations of land surface temperature observed from geostationary satellites, *Geophys. Res. Lett.*, *35*, L22708, doi:10.1029/2008GL035759.

Vlassova, L., F. Pérez-Cabello, M. R. Mimbrero, R. M. Llovería, and A. García-Martín (2014), Analysis of the relationship between land surface temperature and wildfire severity in a series of landsat images, *Remote Sens.*, *6*, 6136–6162, doi:10.3390/rs6076136.

Wan, Z., P. Wang, and X. Li (2004), Using MODIS land surface temperature and normalized difference vegetation index products for monitoring drought in the southern Great Plains, USA, *Int. J. Remote Sens.*, *25*, 61–72, doi:10.1080/0143116031000115328.

Weng, Q. (2009), Thermal infrared remote sensing for urban climate and environmental studies: Methods, applications, and trends, *ISPRS J. Photogramm. Remote Sens.*, *64*, 335–344, doi:10.1016/j.isprsjprs.2009.03.007.

Weng, Q., D. Lu, and J. Schubring (2004), Estimation of land surface temperature–vegetation abundance relationship for urban heat island studies, *Remote Sens. Environ.*, *89*(4), 467–483, doi:10.1016/j.rse.2003.11.005.

Xiu, A., and J. E. Pleim (2001), Development of a land surface model. Part I: Application in a mesoscale meteorological model, *J. Appl. Meteorol.*, *40*, 192–209, doi:10.1175/1520-0450(2001)040<0192:DOALSM>2.0.CO;2.